Dynamical processes in the mesopause region from OH-airglow and meteor echoes above Longyearbyen

Magnus Johan Isaksen

Master's Thesis in Physics
60 credits

Department of Physics
Faculty of mathematics and natural sciences

UNIVERSITY OF OSLO

and

THE UNVERSITY CENTRE IN SVALBARD

Spring 2018

Dynamical processes in the mesopause region from OH-airglow and meteor echoes above Longyearbyen

Magnus Johan Isaksen

Dynamical processes in the mesopause region from OH-airglow and meteor echoes above Longyearbyen

http://www.duo.uio.no/

Printed: Reprosentralen, University of Oslo

Abstract

During the winter season in the high arctic above Svalbard the sun is below the horizon not contributing to heating of the mesosphere and lower thermosphere (MLT) region (50-100 km). In this region there are no direct mesurments of temperature, neutral air density and wind speeds, the only way of getting these parameters are to infer them indirectly by measuring thing such as airglow and metor ablations. The OH-airglow temperature is assumed to have a central emission layer at 87 km while the peak meteor ablation region is at about 90km, both of them are in what is called the mesopause region and relativly close together. Because they are so close toghether they are assumed to be influenced by the same type of dynamics, such as planetary waves and up/downwelling over the pole. The meteor height is used together with a model NRLMSISE-00 in order to find the temperature. The OH-airglow and meteor height are compared to see if they move hand in hand.

The temperatures were seemingly following the same development, but the correlation were below 0,15 for 4 of 6 seasons studied. The end of season of 2008-09 and 2011-12 were found to have a correlation of 0.66 and 0.40 respectively. Both seasons show a stable and denser air-mass after a sudden stratospheric warming, as seen by the meteor height being around 87 km for 2008-09 and around 89 km for 2011-12 for an extended period of time after the event and thing return to normal. Typically there was a cooling observed from November until January, cooling by around 20 K for the OH-airglow temperature and around 10 K for the meteor heights. There were larger variations observed in the OH-airglow temperature by 20-30 K compared to the variations in meteor height temperature 10 K. The OH-airglow variations were also changing quicker, and the meteor height and model used a couple of days to catch up to the rapid changes observed in OH-airglow. The model also did not respond as much to the events of SSW as the OH-airglow. The rapid changes in temperature compared to the meteor heights is most likely the reason for the low correlation. The moving meteor height is also thought to compensate for changes in temperature, density and other factors, while the OH-airglow is assumed stationary and therefore lacking the compensation mechanism generating the large difference seen in temperature.

Acknowledgments

I have had the privilege of conducting the research for my master´s thesis at the University Centre i Svalbard surrounded by the best nature has to offer. This past year has been very educational and submitting this thesis is great achievement and I would like to acknowledge some people that helped me get there.
First and foremost, I would like to express my deepest gratitude to my main supervisor Dr. Noora Partamies for excellent guidance, support and enlightening discussions.
I would also like to offer my appreciation to Dr. Lasse Clausen at my home institution for co-supervising me.
Before starting this thesis, I was given the opportunity to work as an engineer at the Svalbard Satellite Station. I have encountered many great colleagues and friends which made my stay in Longyearbyen a pleasure. I am now looking forward to continue working in the space industry for Svalsat.
And finally I would like to thank Natalie for all the support and help given during this year. For the help in reading and correcting the text and for the fun times shared during our stay at Svalbard.

Contents

Chapter 1

Introduction

The middle atmosphere is one of the less understood regions of Earth's atmosphere. In the lower atmosphere there are tools such as planes, balloons and weather stations which can be used to do direct measurements of temperature, density, pressure, compositions and wind speed. In the upper atmosphere satellites orbit and can do direct measurements. In the middle atmosphere the only way to do direct measurements are rockets, but they only give a brief glimpse of what the conditions are like and are expensive and hard to use. So for the middle atmosphere, indirect measurements are the only way to get information about the region between the lower areas where planes travel and the higher regions where satellites orbit. Recently this region has gained more interest due to climate change and human emissions of greenhouse gases. The part of the middle atmosphere stretching from 50 km to a 100 km above ground is called the mesosphere. The upper limit of the mesosphere is called the mesopause region (80-100 km) and can be considered as a boundary between the neutral atmosphere and the ionosphere. There are large differences in the behavior of atoms and molecules above and below the mesopause region. Below this mesopause region, the main transport mechanisms are winds and turbulent eddies. Above the mesopause region, the transport is mainly done by diffusion from regions of high concentration to regions of lower concentration (Holmen, 2016). The ionized part of the thermosphere (ionosphere) is highly influenced by electric and magnetic fields, and also particle precipitation. The field of ionospheric mechanisms has been studied for decades whereas the neutral atmosphere is less understood with its complex dynamics, photochemistry and heating mechanisms. The interaction between the ionosphere and neutral atmosphere at the boundary heights is a less researched topic that has gained more attention lately. Through vertical motion the atmospheric layers are intimately coupled, but the details of the coupling processes are not well understood. It is important to have reliable long-term weather forecasts for the middle atmosphere to be included in the weather models, and that alone requires solid understanding of the middle atmospheric processes.

This thesis will focus on two methods of observing the mesopause region. First method is by observing a phenomena called airglow. It can be observed from the ground with optical instruments, but is hard to spot as it is diffuse and does not have clear structures

such as the aurora. Airglow, like the aurora is caused by photons emitted from atoms and molecules after they have been exited by radiation or particle precipitation. By measuring the airglow it is possible to find the temperature of the region. The second method is to use a radar to monitor meteors entering the atmosphere. As the meteors enter the atmosphere they are lit on fire and burn up which is referred to as meteor ablation. The meteors will typically burn up in the mesopause region. By using a radar it is possible to determine the ablation height and by comparing with models also the temperature can be found. As both the OH-airglow layer at around 87 km and the meteor peak ablation region around 90 km is close to each other it is possible to think that they will be affected by the same movements in the region. If the entire polar mesosphere is moved adiabatically up and down from downwelling/upwelling, the peak meteor height should correspond to changes in OH-airglow temperature as the region heats and cool. From this the measured peak meteor height could be used as a proxy for the OH layer height.

The thesis will start by exploring the necessary scientific background regarding the atmosphere of the Earth, and understanding the mechanisms affecting the changes in the mesosphere and mesopause both externally and internally. Next, the methods and the instruments used in this study will be presented. Finally, the obtained results will be reviewed and discussed.

Chapter 2

Scientific Background

2.1 Earth's atmosphere

The atmosphere of the Earth can be divided into multiple layers based on different parameters. A typical way to characterize the atmospheric layers is by their temperature, as shown in Figure 2.1. These layers are named the troposphere, stratosphere, mesosphere and thermosphere (ionosphere), respectively. The troposphere is the lowest region stretching up to approximately 10 km, with decreasing temperatures due to radiative cooling. At this altitude a broad minimum in temperature called the tropopause is found. Above the tropopause the temperature starts rising again due to absorption of solar UV radiation, this region is called the stratosphere. At 50 km the temperature starts decreasing again, marking the upper boundary of the stratosphere, called the stratopause. The temperature falls again due to radiative cooling up to approximately 80-90 km altitude. This region of decreasing temperatures is the mesosphere, and the minimum is found as a broad region around 85 km which is the mesopause. Above this region the temperature increases drastically in the thermosphere, this is mainly due to absorption of solar UV radiation and lack of effective heat loss processes (Prolss, 2004).

Due to UV radiation and energetic particle precipitation, particles in the upper atmosphere are ionized. In the thermosphere the density also becomes low enough so that particles can stay ionized for a long time, creating electric fields and currents. This region is often called the ionosphere and the motion is mainly dependent of the magnetic and electric fields. Neutral winds and waves do not influence this region as they do further down in the atmosphere. Below 90-100 km altitude, the amount of ionized particles is low compared to the neutrals, and the mean free path of the particles is not long enough for currents, electric fields and magnetic fields to play a major part in the dynamics. Therefore it is sensible to talk about the neutral atmosphere below 100 km and the ionosphere above.

For convenience, the mesosphere and lower thermosphere region (MLT), from 50km to 100 km, is divided again into smaller regions. The region from 50 km to 79 km will be

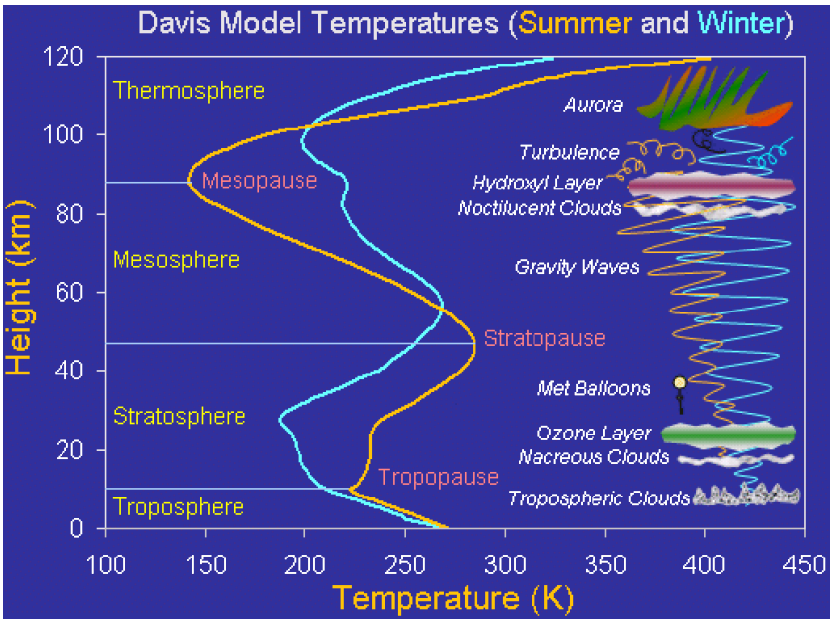

Figure 2.1: Summer (orange) and winter (blue) temperatures of the atmosphere from the MSIS empirical model at the Davis station in Antarctica (68 °34′ S , 77°58′ E). Hydroxl airglow, noctilucent clouds and aurora are indicated at approximate heights of occurrence. Made by John French (French)

called the mesosphere and from 80 km to 100 km will be called the mesopause region. The mesosphere is then divided into the lower mesosphere from 50 km to 70 km and the upper mesosphere from 70 km to 79 km. The mesopause region is divided into the lower mesopause region from 80 km to 90 km and the upper mesopause region from 91 km to 100 km (Beig, 2011).

The mesopause region is one of the less understood regions of the atmosphere, due to the lack of direct observations. Weather balloons and airplanes do not reach higher than the stratosphere, while satellites orbit from 180 km altitude and upwards. All of these methods of measurement only give indirect interference of temperature and wind speed. In situ measurements can be done using sounding rockets, but they are expensive and only give a short glimpse of the conditions. Although direct measurements are difficult, phenomena such as airglow, meteor ablations and polar mesospheric clouds occurring in the mesopause region can be used to derive different parameters (Holmen, 2016; Sigernes et al., 2003).

Airglow is emission of light by excited atoms and molecules in the atmosphere. There is airglow both during the day called dayglow and during the night called nightglow. But only the nightglow is studied in this thesis and will be refered to as airglow from now (See section 2.3).
Meteors are small rocks or dust (1μm to 1m) hitting the atmosphere. When they hit the atmosphere the friction will start to heat them up, and in the MLT region, the density is high enough for the meteors to start burning. This is called meteor ablation (See section 2.4).

Polar mesospheric clouds are water ice crystals formed during the cold summer mesosphere at around 82 km altitude. They are highly reflective and can be sunlit during twilight and are therefore often called noctilucent clouds (Hervig et al., 2001).

2.1.1 Dynamics and temperature variations

Temperature and dynamics in the MLT region is influenced by many different sources such as meridional flow, planetary waves, gravity waves, ozone depletion and solar flux (Holmen et al., 2014b). During the past decades, the temperature in the MLT region has been decreasing (Holmen et al., 2014b; Sigernes et al., 2003).

At higher altitudes, only the lighter atmospheric atoms and molecules survive. At around 80-100 km, the main species are O_3 (ozone), O_2 (molecular oxygen), O (atomic oxygen), H_2O (water), H (hydrogen) and CO_2. Ozone and oxygen are important due to their ability to absorb UV radiation and heating the region, while CO_2 contributes to strong radiative cooling (Holmen et al., 2016). As shown in Figure 2.2, single hydrogen and oxygen/hydrogen and oxygen atoms become more important for chemical processes at higher altitudes.

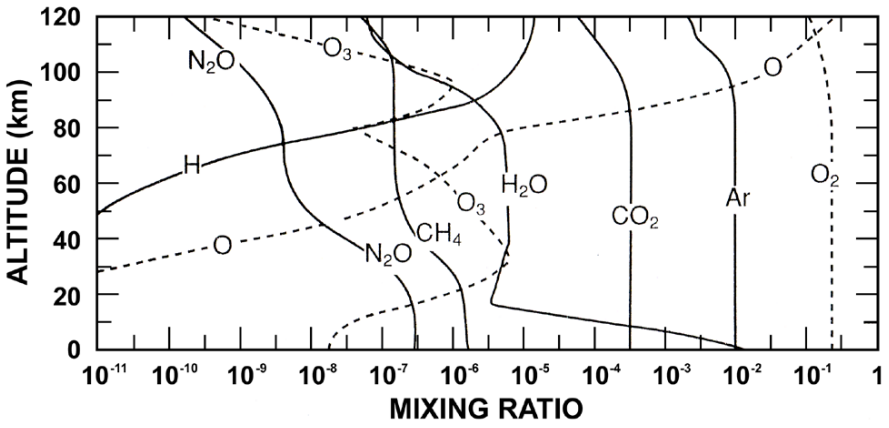

Figure 2.2: Mixing ratio of neutrals in the atmosphere. The mixing ratio is the number density of one gas per density of dry air. N_2 has a stable mixing ratio of 0.78. Source: (Brasseur et al., 1999)

Breaking of tidal, planetary waves and gravity waves control the large-scale circulation and generate vertical motion leading to adiabatic heating/cooling in the MLT region (Holmen et al., 2014b; Becker, 2012). Downwelling above the winter pole causes adiabatically heating and compression of the air. While an upwelling in the summer causes the air to expand and cool. This upwelling and downwelling makes the winter mesopause warmer than the summer mesopause, as seen in Figure 2.1. The downwelling also causes the winter mesopause to be denser than the summer mesopause. (Holmen, 2016; Yi et al., 2018).

Gravity waves (GW) are waves generated in the troposphere by instabilities from disturbances such as thunderstorm updrafts and Kelvin-Helmholz instabilities around the

jet stream. Propagation of these waves is always against the zonal flow, and they can propagate both vertically and horizontally. In the winter, the GWs propagate westward due to the mean stratospheric zonal flow being eastward. (Holmen, 2016)

Planetary waves (PW) or Rossby waves are generated in the troposphere by large scale topography or thermal contrast, by meridional perturbations of the zonal flow. PWs can only propagate westwards. During the Northern Hemisphere winter the mean zonal wind is eastward so the PWs can propagate into the MLT region, but during the summer the mean zonal wind is westward preventing the PWs from propagating in the MLT region. Because the PWs only propagate upwards in winter, the Northern Hemisphere winter is more dynamic than the summer (Holmen, 2016).

A key feature in the large-scale dynamics and temperature in the winter hemisphere is the so-called polar vortex. Above the poles a polar vortex is formed during winter, due to decreasing temperatures and an increasing temperature gradient between the poles and equator. The decreasing temperature is due to a lack of solar radiation being absorbed by ozone. In the summer there is continuous radiation from the Sun and the ozone will absorb much more. This leads to an increased temperature above the pole, and a decrease in the gradient towards the equatorial regions (Holmen, 2016). Inside the vortex the air is sheltered from the waves and mixing with other air masses, this results in a stable air mass and isolated chemistry (Schoeberl et al., 1992).

2.1.2 Sudden stratospheric warming (SSW)

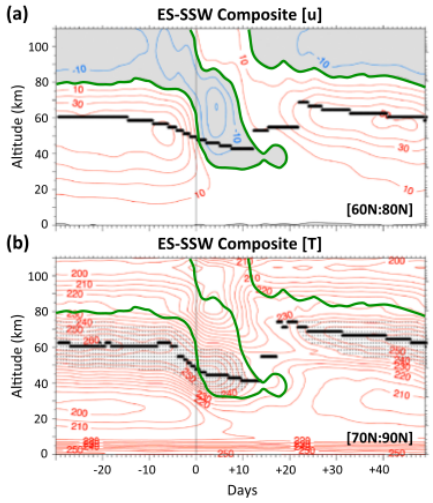

Figure 2.3: Altitude and time section for the development of a SSW. a) zonal mean wind and b) temperature Source: (Limpasuvan et al., 2016)

Sudden stratospheric warming (SSW) is a result of PWs propagating from the troposphere into the stratosphere, and is therefore a winter phenomenon (Dowdy et al., 2004). Large amplitude PWs can propagate poleward and penetrate into the stratosphere (Limpasuvan et al., 2016). SSWs mainly occur on the northern hemisphere due to the distribution of land and sea masses, as the more broken terrain in the Northern Hemiphere generate more PWs. Only one major SSW is recorded in the southern hemisphere in 2002 (Pedatella et al., 2018; Dowdy et al., 2004). Typically a SSW starts with a rapid warming in the stratosphere and a reversal of zonal-wind direction. Also a rapid cooling of the mesopause region is a sign of a SSW. After the onset the system returns to normal, but slower than at onset.

The frequency of the SSWs is about twice every three years or 6 times per decade, depending on long-term variations such

as the El Niño-Southern Oscillation and solar activity (Pedatella et al., 2018; Labitzke, 1987).

The time development of a SSW in the MLT region is shown in Figure 2.3, which is a composition of several cases of elevated stratopause SSWs (ES-SSW). It is an average over the latitudes shown in the lower right corner, between 60°N and 80°N for the zonal wind and between 70°N and 90°N for the temperature. Before the onset at Day 0 the mesospause region starts cooling, while the upper stratosphere and lower mesosphere start warming up. Approximately 10 days before day 0, the wind below 80 km rapidly weakens. At onset a wind reversal takes place as seen in Figure 2.3a, and the wind turns westward. After about 15 days the wind turns eastward again. During onset, the mesospheric temperature rapidly increases, while the mesopause is cooling. 10 days after, the mesopause also starts warming, reaching the highest temperature around day 15. After about 20 days in the upper stratosphere and mesosphere, a new warm layer and the eastward wind picks up strength again returning conditions to normal (Limpasuvan et al., 2016). The average length of a SSW event is considered to be approximately 21 days, with the reversal of the mean zonal wind being the central day of warming (Straus and Stan, 2009).

2.2 Solar activity

The Earth's atmosphere is affected by the sun and the effects caused by solar radiation and the solar wind. The sun releases plasma from its surface which will travel through interplanetary space before arriving at the terrestrial environment. The magnetic field of the sun is "frozen into" the interplanetary plasma, this is called the interplanetary magnetic field, and will interact with the magnetic field of the Earth. UV radiation from the Sun also enters the terrestrial atmosphere, ionizing and exciting atmospheric atoms and molecules. The sun has different cycles of activity influencing its effects on the atmosphere of the Earth. It has a 27 day rotational period permitting different active areas of the solar surface to be facing towards Earth.

The number of sunspots on the solar surface varies with a period of 11 years. This variation is often used as an indicator of solar activity. Sunspots are regions of cold temperature compared to the surroundings, due to strong magnetic fields slowing down convection (Forseth, 2017; Lepping et al., 2003). Another method of measuring solar activity is to use the F10.7 cm solar radio flux, measured in solar flux unit (SFU) at wavelength 10.7cm in 10^{-22} $Wm^{-2}Hz^{-1}$. In response to changes in solar activity the mesosphere changes by an average of 4-5 K/100 SFU, while at higher latitudes the temperature response can be as high at 7-10 K/100 SFU (Gavrilyeva and Ammosov, 2018; Beig et al., 2008). In the high arctic it has been shown that the solar response for the winter season from November to February is around 4 K/100SFU (Holmen et al., 2014a).

As the interplanetary magnetic field interacts with the geomagnetic field and ionosphere, it generates disturbances in the terrestrial magnetic field. The amount of disturbance is then categorized using the K_p index, which is based on observations at primarily middle and high northern latitudes. The value of the K_p index is generated every three hours. The A_p index is a magnetic planetary index based on the K_p in-

dex. While the K_p index is on a quasi-logarithmic scale, ranging from 0 (quiet) to 9 (very disturbed), the A_p index is linear from 0 to 400. This makes the A_p index easier to use when averaging and for sums (Prolss, 2004). The A_p index is therefore used as an indicator of geomagnetic activity. Through energetic particle precipitation, the geomagnetic activity can change the temperature, composition and dynamics of the high latitude atmosphere. Following a geomagnetic storm the atmosphere experience ionization, excitation, Joule heating and dissociation processes (Gavrilyeva and Ammosov, 2018; Xu et al., 2013) which can lead to increasing temperatures in the MLT region.

2.3 Airglow

Airglow is a common name for light emissions in the atmosphere from photochemical processes. Airglow is usually homogeneous and quite hard to observe from the ground. During daytime the phenomena is called dayglow and consists of scattered radiation. During the night it is called nightglow, and is due to chemical flourescence (Prolss, 2004). During this study the nightglow is the more important, and is therefore what is referred to as airglow. Airglow can be generated by several species of atoms and molecules, with the OH (hydroxyl) molecule giving the strongest emission. On average the OH airglow layer can be found at around 87 km altitude. This has to do with the production and loss mechanisms. The fall in concentration of ozone with height and more frequent collisions lower in the atmosphere is part of the limiting factor of where the OH-layer is situated and the mean thickness of around 8 km.

During sunlit hours atomic oxygen (O) is created through photodissociation of molecular oxygen O_2, by extreme ultra violet radiation (EUV) from the sun. The atomic oxygen does not easily recombine and therefore has a long lifetime in the mesopause region, this allows atomic oxygen (O) to be transported from the dayside to the nightside and into the polar night. From Figure 2.2 it is possible to see that atomic oxygen and atomic hydrogen gets more important at higher altitudes, as their mixing ratio increases. The main production of excited hydroxyl OH^* is given in Equations 2.1 (ozone-hydrogen) and 2.2 (Perhydroxyl-oxygen). Globally the ozone-hydrogen mechanism is considered the dominant source of OH^* (Holmen, 2016; Bates and Nicolet, 1950). In polar night conditions however the perhydroxyl-oxygen mechanism is the source of up to half of the OH^* (Holmen, 2016; Sivjee and Hamwey, 1987). These two mechanisms are relying on mixing with atomic oxygen or hydrogen, together with ozone and HO_2. From Figure 2.2 the region more likely for these processes to happen is between 80 km and 100 km, than further down. Above 100 km the ozone and HO_2 mixing ratio decreases rapidly, limiting the thickness of the airglow layer.

$$H + O_3 \rightarrow OH^* + O_2 \tag{2.1}$$

$$HO_2 + O \rightarrow OH^* + O_2 \tag{2.2}$$

The OH airglow emission comes from the rotational and vibrational excited state of the hydroxyl molecule. For a diatomic molecule such as OH, there are several movements and energy levels. Excitation brings the molecule from the ground state denoted by $''$,

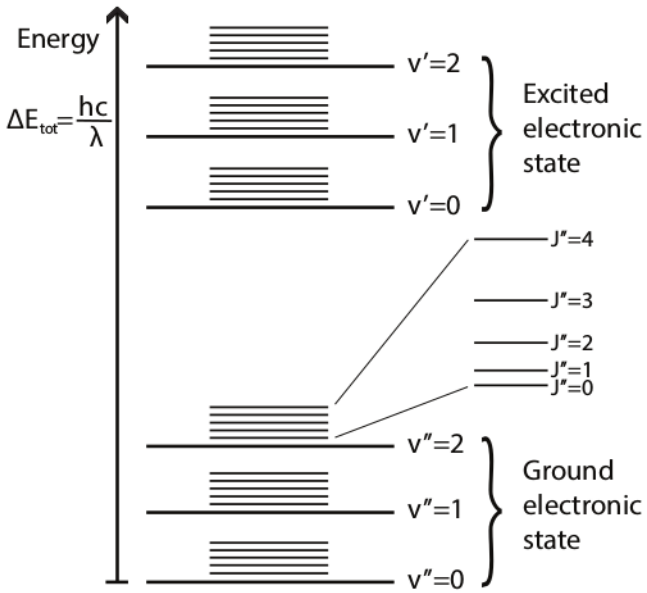

Figure 2.4: Energy levels of a diatomic atom. The electronic levels are separated widely, the vibrational levels v are closer and the rotational levels j are even closer together (Holmen, 2016)

to a higher energy state denoted by $'$, as illustrated in Figure 2.4. The diatomic molecule also have two movements, it can rotate around an axis in the center of gravity and the two atoms can vibrate relative to each other. Vibrational energy is small energy steps in denoted with v in the figure, while rotational energies are denoted with a letter j. The wavelength of emission is determined by the energy transition from one molecular state to the other given by Equation 2.3. Where ΔE is the difference in energy between the two states, h is Planck's constant, c is the speed of light in a vacuum, E_e is the energy of the electronic configuration, E_v is the nuclear vibration and E_r is the nuclear rotation. (Dyrland, 2010)

$$\Delta E = \frac{hc}{\lambda} = E_e + E_v + E_r \tag{2.3}$$

The transition of OH^*(6-2) is the transition from v′=6 to v″= 2. The emission spectra for this transition is shown with the R,Q and P branch in Figure 2.5. At 844.6 nm there is an emission line of oxygen aurora, which can interfere when measuring the intensity of these OH^* lines.

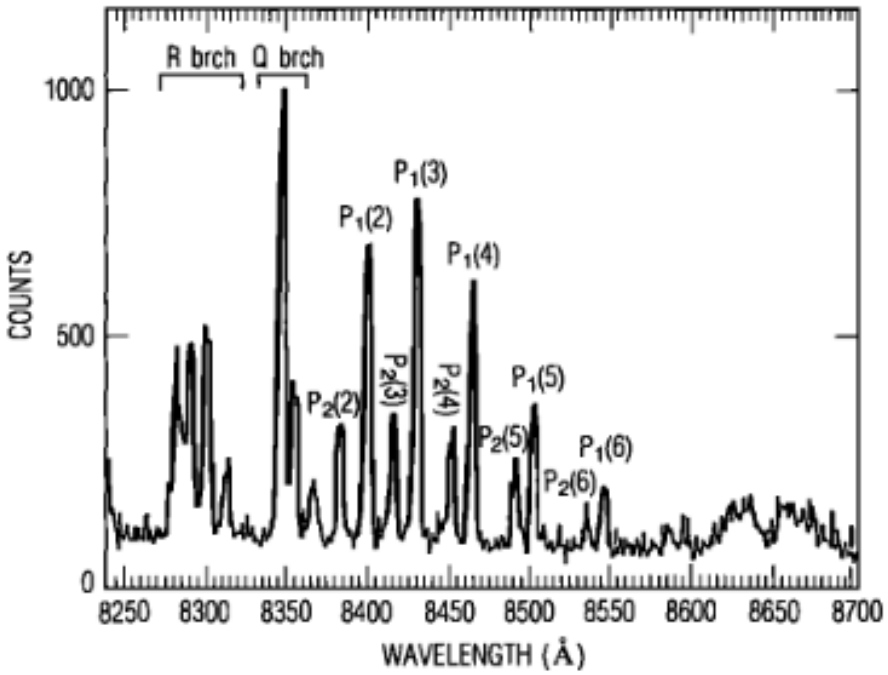

Figure 2.5: Airglow OH(6,2) and O_2 emissions recorded, with a 1/2 m Ebert-Fastie spectrophotometer, at Longyearbyen, (10Å = 1nm) (Sivjee and Hamwey, 1987)

2.4 Meteor ablation

The dust and small fragments of sand that enters the atmosphere are remnants of comets and asteroids that have been floating around in the solar system. Meteoroids are small objects ranging from 10 μm to 1 m, travelling through outer space (Rubin and Grossman, 2010). The debris enters the atmosphere at speeds of 12-72 km/s. Meteoroids colliding with the atmosphere get slowed down by friction, generating heat sufficient to sublime and ionize the atoms and molecules of the surrounding atmosphere. This generates a plasma trail that can be used to determine temperatures and velocities. Meteor ablation is when the meteor looses mass due to sublimation during the descent. From fragmentation and ablation most meteors are destroyed in the MLT region, although a few make it to the surface. The meteoroids that make it to the surface are called meteorites (Dyrland, 2010).

Using the plasma tail of the meteor, radio waves can be sent from the ground and scattered of the plasma particles. Depending on the plasma frequency compared to the radar frequency, the meteor trail can be either underdense or overdense. If it is underdense the radio wave penetrates the tail freely and get scattered by single electrons. If the tail is overdense the wave gets scattered by the surface layer of the trail (Holmen, 2016).

Chapter 3

Instruments and methods

3.1 OH Airglow data

3.1.1 Airglow spectrometer

An Ebert-Fastie spectrometer with a focal length of 1 m, is used to scan the wavelength region 831.2 nm-874.5 nm with a band pass close to 0.5 nm. Corresponding to OH*(6-2) vibrational bands of the airglow. The instrument has a 5°field of view fixed in geographical zenith. The experimental setup of the Ebert-Fastie spectrometer can be seen in Figure 3.1, where the principal components are a spherical 1 m focal length mirror, one plane reflective diffraction grating and a pair of curved slits. The instruments scans the wavelength region every 25 seconds and averages over an hour to get better signal to noise ratio (SNR). This is then used to get the diurnal average used in this study.

The spectrometer is located on the mountain Breinosa at 520 m altitude, close to Longyearbyen. Longyearbyen is without sunlight for 4 months from November through February, making it a good place for diurnal measurements of airglow. Measurements are only taken when the Sun is 10°or more below the horizon (Sigernes et al., 2003).

3.1.2 Usage of the OH^*(6-2) airglow data

Airglow is used for approximating temperature within the OH layer, centered at around 87km. The temperature of OH*(6-2) is derived using the relative intensities of the rotational lines. Highly exited rotational states of OH^* are produced during the reaction in Equation (2.1), this gives a short non-Boltzmann distribution of energies with a short lifetime. Local thermal equilibrium can be assumed due to $OH^*(v' > 2)$ undergoing 10 or more collisions before releasing a photon (Holmen, 2016; Sivjee, 1992). After assuming thermal equilibrium a Boltzmann distribution can be used to find the probability of a system being in a certain state, this is then a function of the state's energy

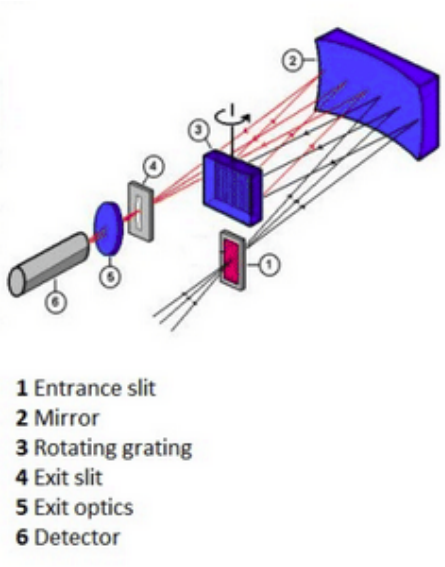

Figure 3.1: Ebert-Fastie spectrometer setup

and the system's temperature. From this it is possible to find a linear relation between the intensity and rotational term, this linear relation can be used to find the rotational temperature. And because the system is assumed in thermal equilibrium this is close to the neutral temperature of the mesopause region. For a full description of how to find the rotational temperature see chapter 3.3 in (Holmen, 2016).

The spectrometer is sensitive to light pollution from sources such as the Moon, the town and northern lights. The aurora is dynamic and can be in direct field of view of the instrument. As mentioned in 2.3, the oxygen line at 844.6 nm is in the middle of the OH^*(6-2) bands. This generates challenges with the measurements since the aurora may have a higher intensity than the airglow. This light pollution is a source of uncertainty and can give errors in the measured data.

In this study, the OH-airglow temperature is compared to the model temperatures corresponding to the heights of the meteor peak flux from the meteor radar described in Section 3.2. This is done for several seasons defined by the period of measurements for the OH-airglow data, usually from November to February.

3.2 Meteor radar data

The Meteor ablation data is measured by the The Nippon/Norway Svalbard Meteor Radar (NSMR) located in Adventdalen at 78.33°N and 16.00°E. Operating at 31 MHz, the NSMR transmission is at 7.5 kW peak power circular polarization using a three-element crossed Yagi (Hall et al., 2006, 2002). The radar sends out a signal which is reflected by the plasma trail of the meteor, as illustrated in Figure 3.2 by the conventional meteor radar and meteor trail echo. Phase differences of the received signal on

the different antennas are used to determine the position for the meteor in the sky. The range resolution of the radar is 1 km (Dyrland, 2010). From the range and position it is possible to calculate the height distribution of the meteors. A typical day has around 5 000 meteor echoes and a peak ablation height of around 90 km. Typically there is around 100-300 echoes per hour, allowing for a time resolution of an hour (Dyrland et al., 2010a).

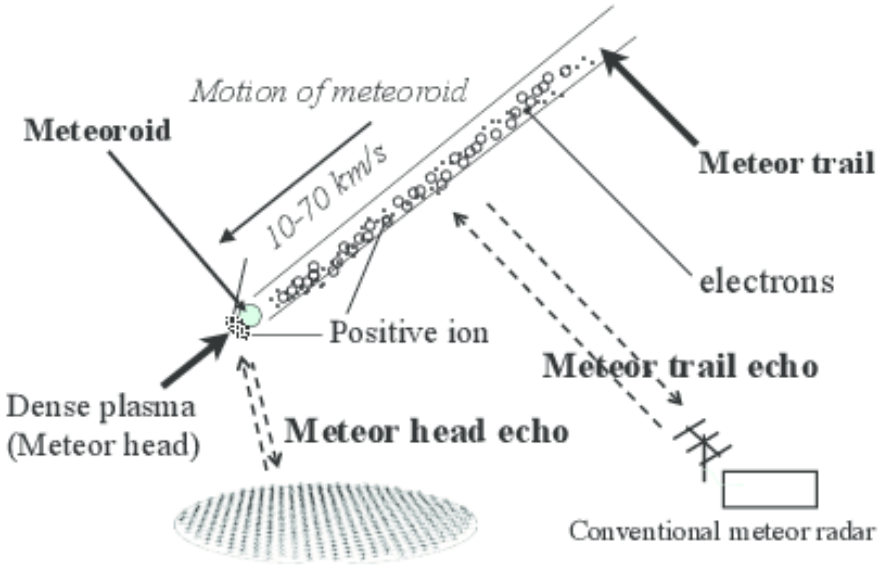

Figure 3.2: Schematic of meteor trail echo (Abe et al., 2015)

3.3 Data Processing

Two main data sets are used, the airglow temperatures and the meteor ablation height. Other data sets include the A_p and F10.7 index from OmniWeb (NASA, 2018). The A_p index is used as an indicator of the disturbances in the terrestrial magnetic field, which is influenced by the charged particles in particular at polar latitudes. Due to collisions energy can be transferred between ionized particles and neutrals, increasing or decreasing the temperature in the region. Disturbances in the magnetic field can channel energy into the ionized particles due to them being ”frozen-in” the magnetic field.

The programme gathers the data and sorts them into winter seasons. Then the programme is used to plot height and temperature measurements in comparable format on the same time scale. When the main data sets are read, the programme uses the NRMLSISE-00 model in order to convert the height distributions from the radar into corresponding temperature values from the model atmosphere. To do this a Gaussian

fit is used to determine the maximum ablation height from the meteor flux profiles for the model input.

3.3.1 Gaussian curve fit

In order to get a cleaner picture of at which altitude most of the meteor echoes occur a Gaussian fit was implemented. This Gaussian fit smooths the curve and gives a representative height for the meteor flux. This fit tries different parameter until it finds a good fit, but is limited to 1000 tries in order to save time running the code. A few days only have one or two data points and the curve fit then doesn't find a fit.

$$F(x) = A * e^{\frac{-(x-x_0)^2}{2\sigma^2}} \tag{3.1}$$

The Gauss function 3.1 is using the curve fit function from the package Scipy in Python, to find the best possible fit to the measurements. In the Gaussian function x is the measured value, x_0 is the average value gotten from the distribution, σ^2 is the variance and A is a constant used to move the curve away from 0 and set the curve above the measurements. When it finds a fit as in Figure 3.3 it finds the height of maximum ablation. The fitted maximum is then used as the height sent in to the NRLMSISE-00 model described in Section 3.3.2

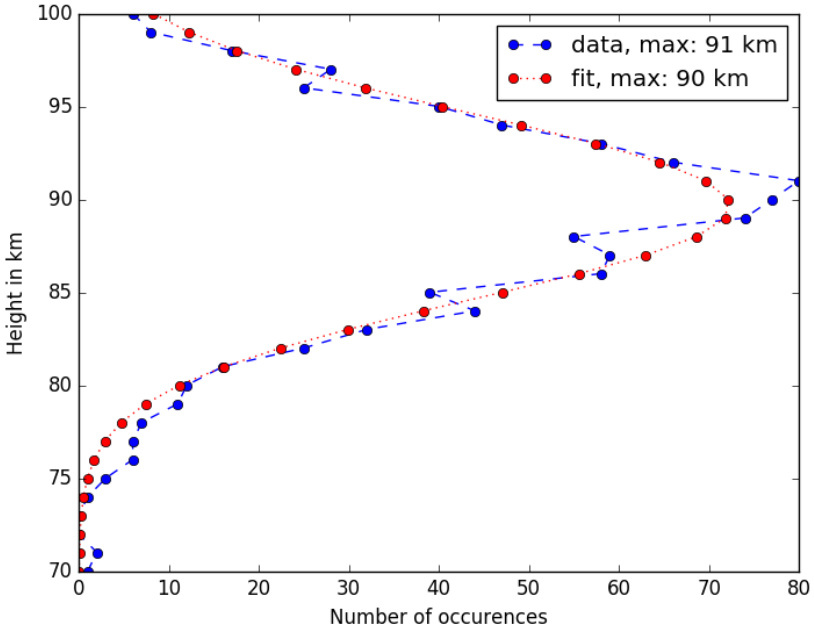

Figure 3.3: Fitting of Gauss curve to the height measurements of meteor ablation

In some cases no fit to the Gaussian curve is found, as is the case on 16.02.2014 in Figure 3.4, where there were not enough data point to provide a fit. The model require

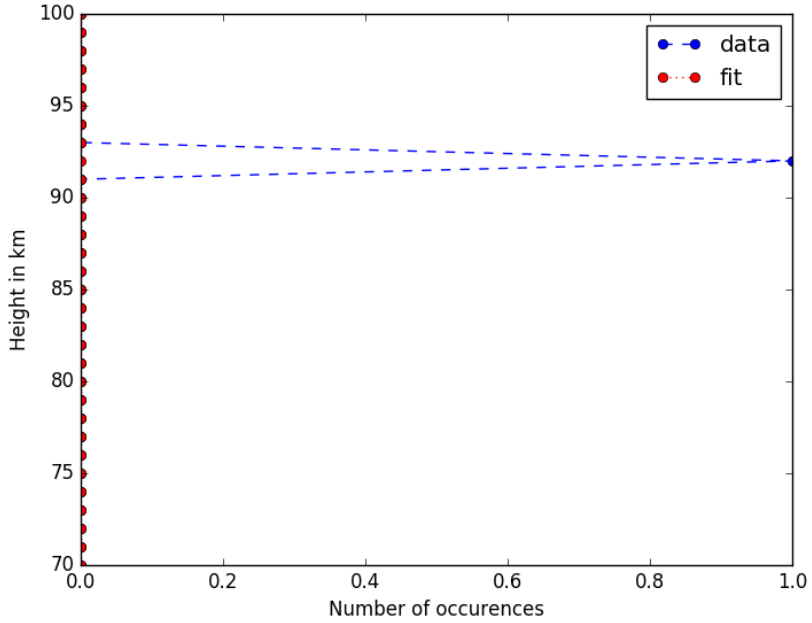

Figure 3.4: Attempted fit to gaussian curve, where the program could not find a good fit. Date 16.02.2014

at least 2 points that are not to far apart in order to get a reasonable fit. When this happens it tries to find values to use in the Gaussian function fails to do so, and it reaches the maximum number of tries allowed. If there is no fit found the value of the height is set to 70 km to mark it as an anomaly, 70 km is chosen as this is the lower boundary of the measurement region. Also the model did not compile if the value were set to NaN, while setting the anomalies to 0 made a very large impact on the temperature, and setting the anomalies to 70 km clearly marks them.

3.3.2 The atmospheric model NRLMSISE-00

The NRLMSISE-00 atmospheric model is an empirical model, based on the two models MSIS-90 and Jaccia-70 (Picone et al., 2002). The model describes the statistical averages profiles of neutral temperature and density from the ground to the thermosphere at any given local and time.

After finding the height of maximum number of meteor echoes, the NRLMSISE-00 model is used to calculate the temperature. This is done by sending in the height, the A_p index and the F10.7 cm index. The model then returns the temperature of this height region.

In the NRLMSISE-00 model the A_p and F10.7 cm indices are considered to not play a major role below 80 km of altitude. As the airglow and typical meteor burnout region

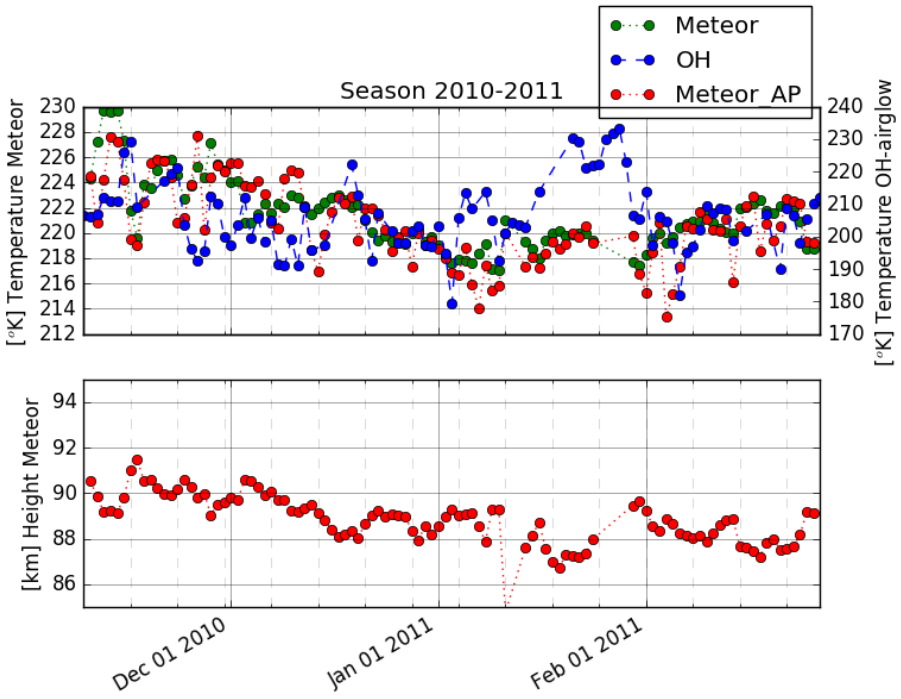

Figure 3.5: Seasonal plot 2010-2011. Top panels show meteor temperature without A_p and F10.7 cm indices included in green, meteor temperature with A_p and F10.7 cm indices included in red and OH-airglow temperature in blue. Second panel shows the height of meteor ablation.

is from 85 to 95 km altitude, the temperature is affected by the solar flux and variations in the geomagnetic activity. This region is at the boundary between the mesosphere and thermosphere (ionosphere), in this region the ionized particles have the opportunity to move a considerable distance before being quenched. The fact that they can move more freely than lower down in the atmosphere also let them be more affected by magnetic activity. In Figure 3.5 the OH-airglow temperature and the model temperature is plotted with and without including the A_p and F10.7 cm indices. The meteor height derived temperature (labelled as Meteor) is produced without A_p and F10.7 cm indices and is smoother without transient temperature changes. This represents the more empirical model and does not follow the evolution of the OH-airglow temperature. When A_p and F10.7 cm indices are included (labelled as Meteor AP), the model produces larger temperature variations, and seems to follow the OH-airglow temperature to a better degree. And because the height is usually around 90 km altitude the additional information by A_p and F10.7 cm indices is an important factor to include in the model.

Chapter 4

Results and analysis

Optical OH-airglow data from 2008 to 2015 was measured by the Ebert-Fastie spectrometer at the Kjell Henriksen Observatory (KHO) on Svalbard. These data sets provide a neutral temperature based on the airglow intensity (see 3.1.2). A diurnal mean of OH-airglow measurements is then compared with meteor radar data. As Svalbard is located on high latitudes, it is exposed to seasonal light variations with the polar night (Sun below the horizon) from November to March. This total darkness facilitates the optical observation of the high intensity wavelengths of OH-airglow 24 hours per day. On the other hand, radar measurements are not limited to any season. In this study, data from the the Nippon/Norway Svalbard Meteor Radar (NSMR) located in Adventdalen is utilized. These measurements give a height distribution of meteor ablation, where the height of the maximum number of ablations (found from a fitted Gaussian curve to the distribution) during the day is used to find the temperature from NRMLSISE-00 model.

Seasons before 2008 are found to have too few measurements for OH-airglow, making the data sets not comparable to the meteor alation measurements. Season 2009-2010 is also not considered because of the lack of OH-airglow measurements. The seasons from 2010-2011 until 2014-2015 all contain comparable data sets from both OH-airglow and meteor radar. Therefore the season of 2008-2009 and the seasons from 2010-2011 until the 2014-2015 are chosen for further study.

In Figure 4.1 the number of data points for the OH-airglow measurements are low until the end of January, making the data sets not easily comparable. From the end of January until the end of the season both data sets provide a good amount of data. In this period both the OH-airglow temperature and the temperature derived from the height of maximum ablation follow the same development. Note that there is a difference in scaling on the two axis, so the OH-airglow temperature is at the right axis, while the modelled temperature based on the meteor height is on the left. The meteor temperature is higher at around 222 K, while the OH-airglow temperature is around 200 K during the period from the beginning of February and to the end of the season. Looking at the lower pane in Figure 4.1 the height in this period is quite stable at around 87 km altitude.

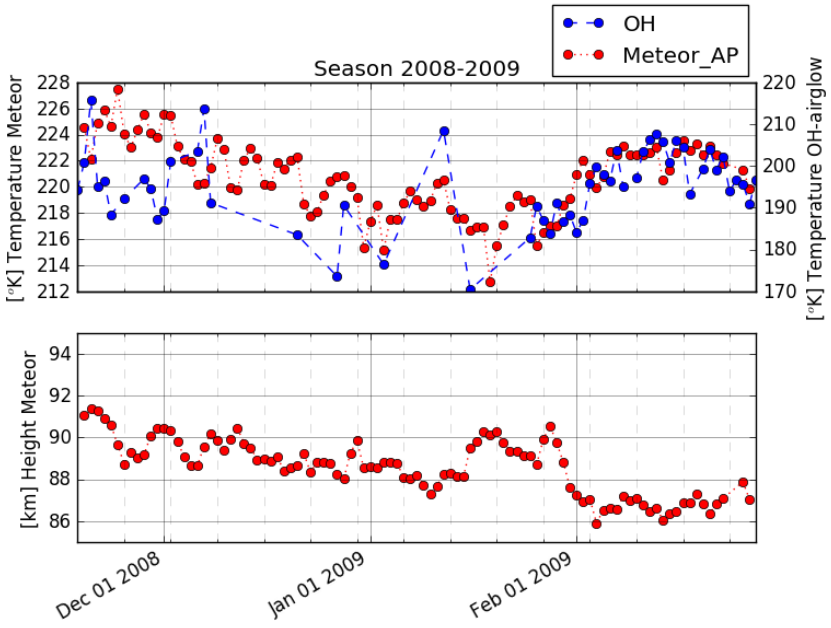

Figure 4.1: Season 2008-2009. Time series of A_p and F10.7 cm indices corrected temperature from meteor height and OH-airglow temperature in top panel. In the lower panel is a time series for the meteor ablation height

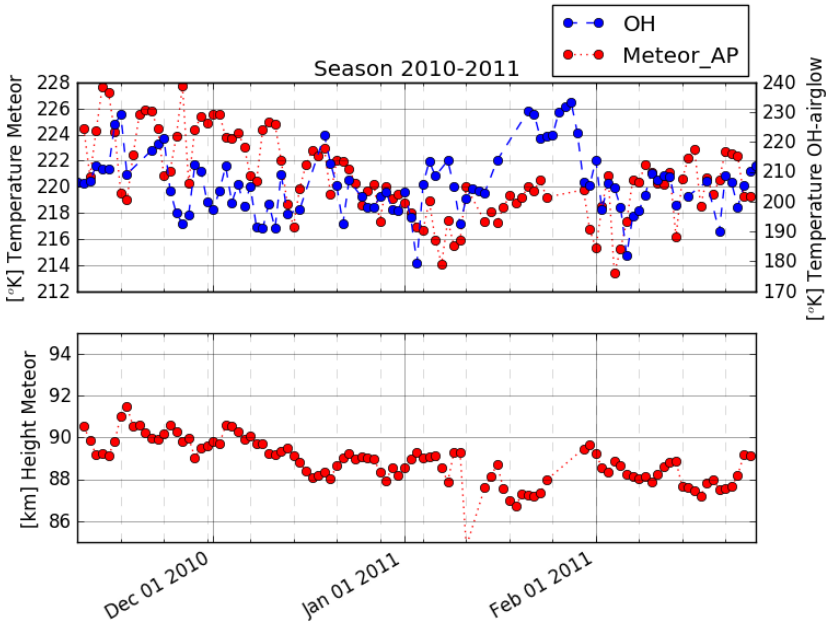

Figure 4.2: Season 2010-2011. Time series of A_p and F10.7 cm indices corrected temperature from meteor height and OH-airglow temperature in top panel. In the lower panel is a time series for the meteor ablation height

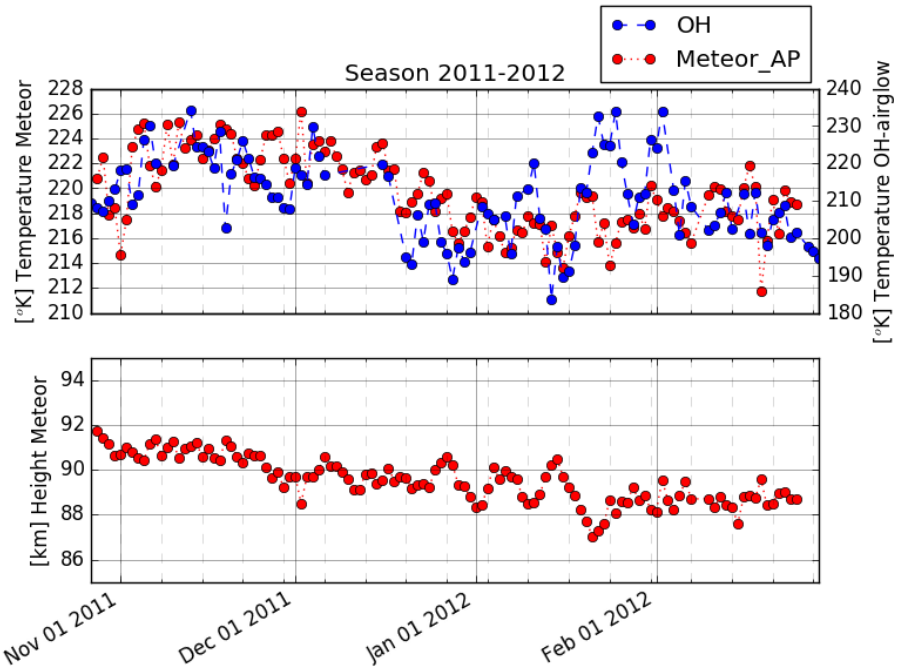

Figure 4.3: Season 2011-2012. Time series of A_p and F10.7 cm indices corrected temperature from meteor height and OH-airglow temperature in top panel. In the lower panel is a time series for the meteor ablation height

In the beginning of the 2010-2011 season shown in Figure 4.2, between November and mid January, the data sets seem to follow the same trend. In mid January the OH-airglow temperature gets enhanced from around 200 K to around 230 K. The same thing does not happen for the temperature from the meteor height, although it rises a bit during this period it is not to the same degree as with the OH-airglow temperature. In the time-series for the height of maximum meteor ablation a height decrease can be observed, related to this period. In the beginning of February 2011, the OH-airglow temperature decreases back to around 200 K, following the development also seen in the meteor temperature.

During the 2011-2012 season in Figure 4.3, there can be observed a more day to day change in the temperature of the OH-airglow measurements. As in the previous season 2010-2011 in Figure 4.2, the OH-airglow variations follow the changes in meteor temperature in the beginning of the season. Around mid to end of January the OH temperature changes more rapidly, but the changes in meteor temperature follows but are not as large as in the OH temperatures.

There is an increase in the OH temperature around 10th of January during the 2012-2013 season in Figure 4.4. This increase is not observed in the Meteor temperature. The OH temperature from 200 K to about 240 K in the middle of January this season, while the meteor temperature remains quite stable around 215-220 K. Before this warming seen in the OH-airglow temperature, the two data sets seem to follow each other more closely with similar variations in temperature. In the end of January there is a day

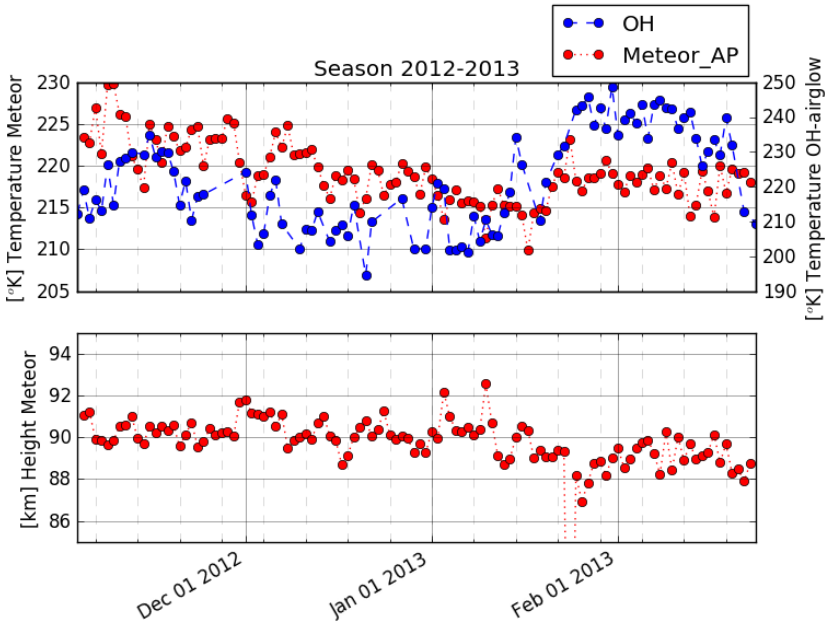

Figure 4.4: Season 2012-2013. Time series of A_p and F10.7 cm indices corrected temperature from meteor height and OH-airglow temperature in top panel. In the lower panel is a time series for the meteor ablation height. One point in the height is outside view, this i a bad fit and the height is put to 70 km

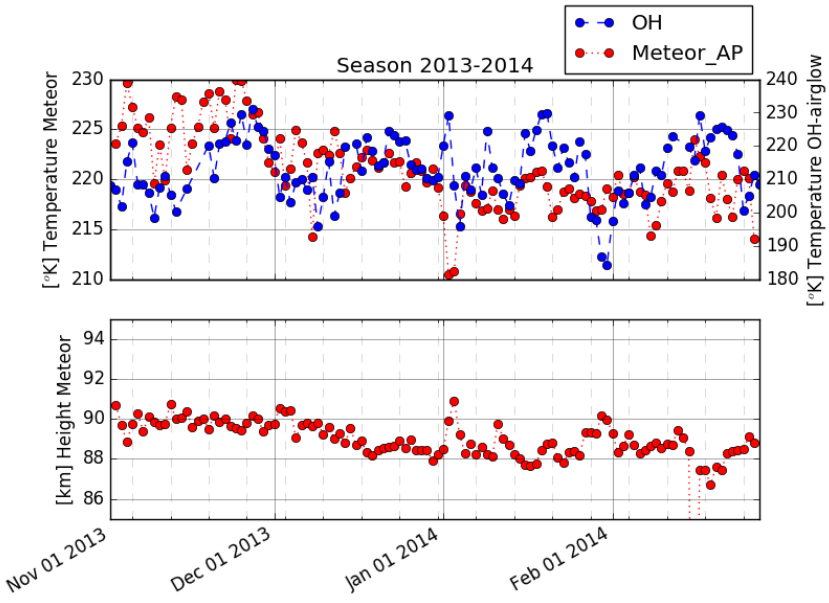

Figure 4.5: Season 2013-2014. Time series of A_p and F10.7 cm indices corrected temperature from meteor height and OH-airglow temperature in top panel. In the lower panel is a time series for the meteor ablation height. One height point in the middle February is outside the figure, this is due to it being a bad fit and the height is therefore sat at 70 km

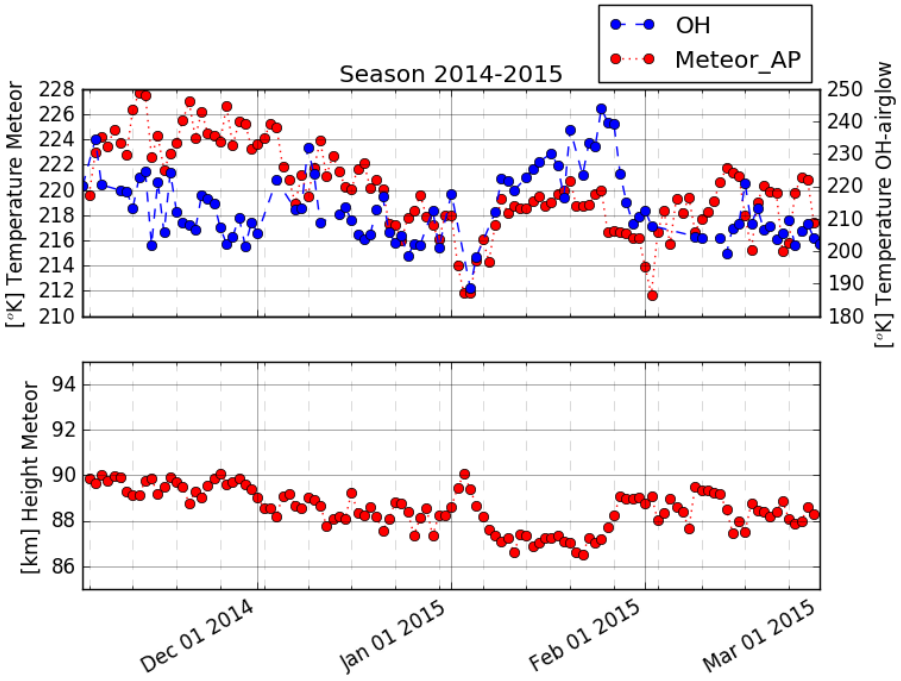

Figure 4.6: Season 2014-2015. Time series of A_p and F10.7 cm indices corrected temperature from meteor height and OH-airglow temperature in top panel. In the lower panel is a time series for the meteor ablation height

where no Gaussian fit was found, when this happens the height is set to 70 km which is much lower than the other values. This error is translated to a rise in temperature by 5 K.

During the season of 2013-2014 in Figure 4.5 the A_p and F10.7 cm indices corrected temperature follow the OH-airglow temperature quite well during November and December. In January the OH-airglow temperature rises up to around 230 K, on several occasions, this change is not observed in the meteor temperature. During this period and the rest of the season, there are large variations between 190 and 230 K in the OH-airglow temperatures, while the changes observed in the meteor temperature are between 215 and 225 K. In the middle of February there is a day where no Gaussian fit was found, as in Figure 4.4 the height is put to 70 km. This error is not easy to see in the temperature, but might cause a slightly elevated temperature.

During the season 2014-2015 the two different data sets follow each other in November and December. In January the OH temperature goes from about 190 K to 220 K during a few days. The meteor temperature also increases from 213 K to 220 K during this period. Both data sets have small decreases in temperature before the the increase is observed. In the period of enhanced OH temperature in January, the maximum height of meteor ablation remains stable as shown in the lower panel in Figure 4.6. When comparing with the other seasons, this stability in ablation height is not commonly observed this late in the season.

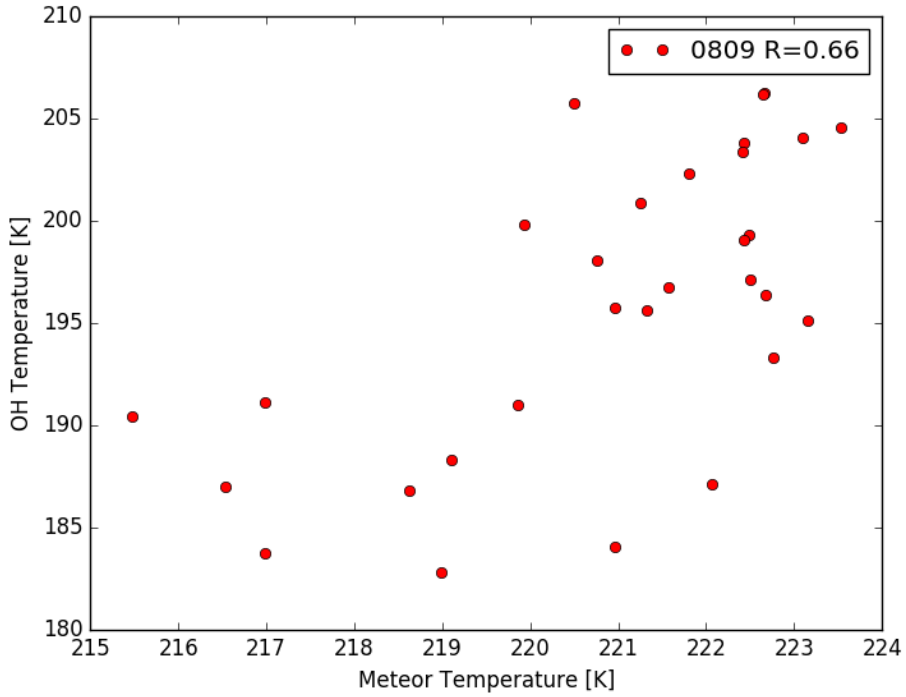

Figure 4.7: Meteor temperature vs OH-airglow temperature, with correlation coefficient R. From 25th of January until the 28th of February in the 2008-2009 season.

Comparing the seasons 2011-12, 2012-13, 2013-14 and 2014-15, they all start out stable with a decrease in temperature until beginning/mid January. From mid to end January the OH-airglow temperature rises fast and the meteor temperature does not follow this development as well in the seasons 2011-12, 2012-13 and 2014-15. In the 2014-15 season in Figure 4.6 this also happens and the changes in the meteor temperature follows the same trend, but not to the extent of the changes happening in the OH-airglow temperature. During this period of rise in temperature the meteor height is stable at 87 km.

For the period from the 25th of January until the 28th of February 2009 the temperature for the A_p and F10.7 cm indices corrected temperature from the meteor ablation height is plotted against the OH-airglow diurnal average temperature in Figure 4.7. The start of the season is excluded due to the lack of OH measurements earlier in the season of 2008-2009. The correlation coefficient R is 0.66, which is higher than the correlation for any other season, shown in Figure 4.8. For the seasons from 2010-2011 until 2014-2015 there is no distinguishable pattern and the correlation coefficients also are low for the respective seasons. Season 2011-2012 has the highest correlation of the full seasons with the coefficient of 0.40, while the remaining seasons have correlation coefficients smaller than 0.15. In Figure 4.3 the season 2011-2012 is shown and it is a more stable season compared to the other seasons we have studied. The OH-airglow temperature does not increase strongly, as in the other seasons. During this season the temperature from both the OH-airglow and meteor data follow a similar trend.

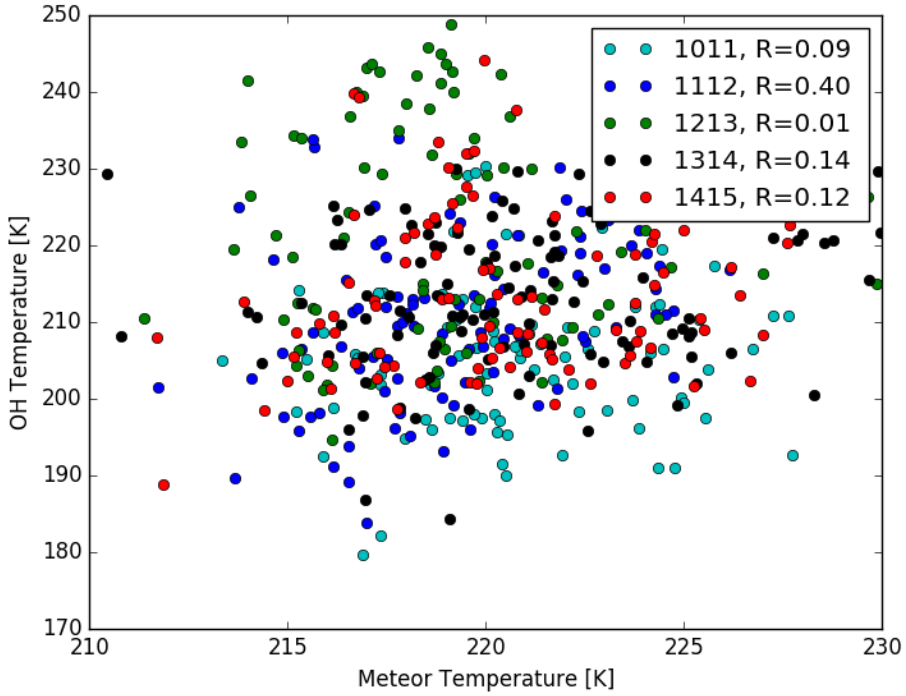

Figure 4.8: Temperature from meteor height against OH-airglow temperature. With correlation coefficient R for each season

Chapter 5

Discussion

During the seasons (November-Mars) from 2010 until 2015 there is typically seen a warming event around January/ February found in the OH-airglow temperature and meteor heights. During the warming event the meteoric temperature from the model follows, but does not keep up the development of the OH-airglow temperature. Temperature variation of 20-30 K was observed in OH-airglow temperature and 10 K observed in meteor height derived temperature. In the beginning of the seasons a negative trend is seen in both the OH-airglow and the meteor temperatures. In the end of October/ beginning of November the sun sets for the polar night in the Svalbard area. During the polar night there is no solar radiation heating the atmosphere, the mesopause region therefore looses heat due to radiative cooling by mesospheric ozone and CO_2. During the winter months the atmosphere compresses from downwelling above the pole, this contributes to heating the mesopause region (see Section 2.1.1). This downwelling and the increased strength of the polar vortex prevents the cooling from happening rapidly during the winter months from November to February. For the seasons 2010 to 2015 the temperature decrease from November to January was about 10 K for the meteor temperature, but the temperature decreased with about 15-20 K for the OH-airglow.

The meteor temperature is usually higher than the OH-airglow temperature, this can be because the OH-airglow temperature assumes a center of the emission layer to be 87 km, while the meteor height changes over time and is usually around 90 km. Temperature from the meteor data is found using the peak height of meteor flux and the NRLMSISE-00 atmospheric model. The assumption of a static OH-airglow emission layer at 87 km is not necessarily a good assumption, as dynamic processes can bring the OH-layer higher or lower in the MLT region. By (Dyrland et al., 2010b), the OH-airglow peak emission height is observed to decrease with as much as 10 km, increasing the temperature with 15 K due to a strong stratospheric vortex. In the mesopause region the temperature gradient can be very steep, so even a small change in the height of peak emission can change the temperature with quite a lot. Typically if the changes in temperature is about 1.5-2 K/km then the difference in height between the two layers should not be seen as a difference of more than 6K, but a difference of up to 20 K is observed. In the beginning of the season the meteor height is mostly stable at around 90-91 km, and then decreases during the winter. This decrease in meteor height can be

Season (Nov-Mar)	**Warming event** (start date)	**Type**	**Identified by**
2008-09	January 21st	ES-SSW	(Limpasuvan et al., 2016)
2010-11			
2011-12	January 13th	ES-SSW	(Limpasuvan et al., 2016)
2012-13	January 5th	ES-SSW	(Limpasuvan et al., 2016)
2013-14			
2014-15	January 4th	Minor-SSW	(Manney et al., 2015)

Table 5.1: Table of identified SSW by date and season

compensating for changes in the air-mass, and be the reason for the meteor temperature does not show as large variations in temperature as the OH-airglow. In a similar fashion as the meteor height changes to compensate for changes it is possible to think that the OH-airglow layer also does that, but this shows up as larger variations in temperature due to the assumption of a static layer at 87 km.

After the period of decreasing temperature there is often a event where the temperature increases rapidly, which can be found in seasons 2008-09, 2011-12, 2012-13 and 2014-15 as shown in Table 5.1.The warming event can be from a major sudden stratospheric warming (SSW) event or a minor sudden stratospheric warming (minor-SSW), the minor-SSW events can be a decrease in the mean zonal wind speed without a full reversal as is the case for a SSW. Both event types are due to planetary and gravity wave activity, reducing the zonal wind speed and weakening the polar vortex.

During the season of 2011-12 in Figure 4.3 there was an elevated stratopause SSW (ES-SSW) starting on January 13th (Limpasuvan et al., 2016). Elevated stratopause event is when the stratopause disappear during an SSW, before returning as things normalize, but at a higher altitude than before. When this happens the stratosphere warms up, but there is a cooling of the mesosphere as seen in Figure 4.3. After the cooling and the SSW mesospheric temperature increases by 30-40K. This is seen in the OH-airglow temperature, but not in NRLMSISE-00. The ablation height remains around the same height as when the event started. Possibly due to the height not being only dependent on temperature, but being dependent on the neutral density, meteoric mass and speed and many other parameters (Hunt et al., 2004). In season 2012-13 in Figure 4.4 the same type of development as for Season 2011-12 is observed. From (Limpasuvan et al., 2016) there is an ES-SSW event on January 5th this year, which might be the reason behind the increased temperature seen around the middle of January. This increase in temperature shows the typical characteristics of a SSW in the mesopause region, with a rapid decrease in temperature a day or two before a large increase in temperature. The meteor ablation also reaches further down in the mesopause region to about 88-89 km. The season of 2013-14 in Figure 4.5 does not show any sign of a SSW. There are some periods of rapid change in temperature and meteor ablation height in January. The observed changes can be from wave activity that does not change the zonal-wind direction, but can weaken the zonal wind. A movement of the polar vortex can also be responsible for the changes observed in height and temperature. The season of 2014-15 in Figure 4.6 shows the traditional seasonal variation with a decrease in temperature starting in November lasting until end of December. Starting at the 4th of January there are typical signs of a SSW in the temperature, first a cooling before a rapid increase in

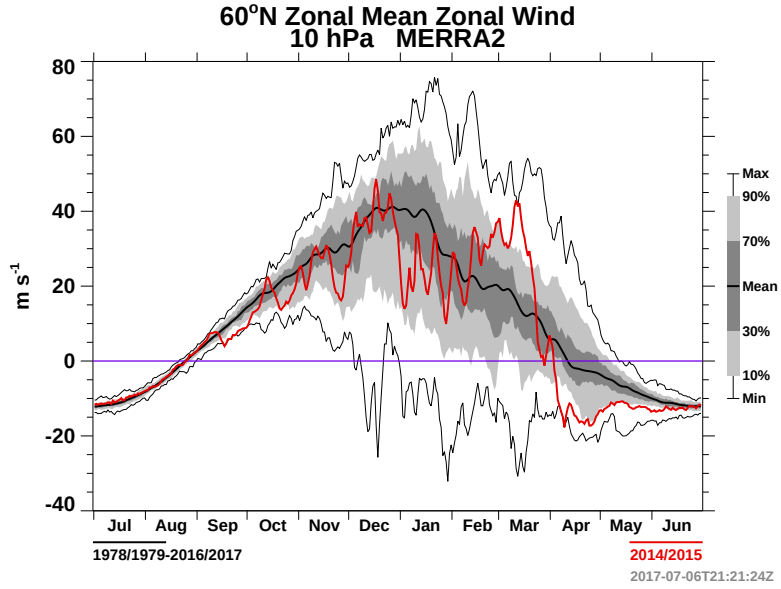

Figure 5.1: Zonal wind at 10 hPa at 60N for the season 2014-15, from Merra 2 (NASA Atmospheric Chemistry and Dynamics Laboratory)

temperature. The temperature increase holds the temperature high for around 20 days, which is the typical length of a SSW (Limpasuvan et al., 2016). For the ablation height there is short decrease in penetration depth, before going further down and stabilizing around 87 km. From the zonal wind data in Figure 5.1 there is no zonal wind reversal seen at 60 °N around the 1st of January, so there is no major SSW in the beginning of January. This season is not discussed by Limpasuvan et al. (2016), but Manney et al. (2015) classifies the event as a minor-SSW. The minor-SSW is a warming event like a SSW, but does only weaken the polar vortex and does not bring a reversal of the mean zonal wind. This event brings a stable and more dense air-mass over Longyearbyen, which is seen in the stable meteor ablation height at around 87 km between January 7th and January 25th. The decrease in height and stability can come from an increased polar vortex strength as the wind speed strengthens again after the minor-SSW event, increasing the downwelling and compressing the atmosphere.

The correlation between the two methods of finding the temperature is small or non existent as seen in Figure 4.8. While four of five seasons in Figure 4.8 have smaller than 0.15 as correlation coefficient, meaning there is no definite connection between the data sets and methods. A season with a higher correlation in Figure 4.8 is the season of 2011-12 with $R = 0.40$. From Figure 4.1 there is another better correlation, with a correlation of $R = 0.66$ between the meteor temperature and the OH-airglow temperature during the end of season 2008-09. Starting in the the end of January 2009, this is in a period when the temperature has increased after a period of decrease in temperature. Together with the stability of the meteor height during this period, it indicates

that not much mixing of air-masses are taking place. According to Limpasuvan et al. (2016) a SSW is taking place on January 21st 2009. This corresponds well with a sudden decrease in the temperature seen around the 20th of January this year. In February the meteor ablation height remains stable at around 87 km giving a good agreement in the evolution of the temperature, although the changes are in the order of 20-30 K for the OH-airglow temperature and 8-10 K for the meteor temperature. The stability in meteor ablation height may be the reason for the better correlation during the last part of the 2008-09 season than for the other seasons studied. Both the season of 2008-09 and 2011-12 experiences a SSW event with stable conditions after, with the meteor height keeping around 87 km for season 2008-09 and around 89 km for the season of 2011-12. The reason for these two seasons to get a better correlation might be because of the stable air-mass after the SSW event. The two methods used during this study seem to follow each other quite well during more stable conditions, when there is less wave activity and abrupt changes. The OH-airglow temperature seems more sensitive to quick changes than the meteor height. That the meteor height is less responsive to quick changes might be due to the meteor height being more dependent on density than temperature, but might also be because the OH-airglow is more responsive to events such as geomagnetic activity and particle precipitation. The OH-airglow also has larger changes in temperature of 30-60 K in the course of a season while the model changes with 10-20 K. This might be because the meteor ablation height measurement implies a temperature according to the statistical model, which probably results in milder temperature changes than those of the real dynamic atmosphere. The model used NRLMSISE-00 is an empirical model based on earlier observations, and although it has become better at including large events such as geomagnetic storms, energetic particle precipitation and SSWs it still has problems with capturing local changes and shorter timescales (Picone et al., 2002). From the diurnal averaging the short substorm and other short lived events is not captured by the OH-airglow either, but storms taking several hours will make a contribution to change in the OH-airglow. The limitations in the model might be one of the challenges in comparing the data-set, as it does not have problems with short term changes and is slow to react.

Conclusion

During this study two methods of finding the temperature in the mesopause region (80-100 km) is used. The teo methods are OH-airglow and meteor echo heights together with an atmospheric model NRLMSISE-00. During the seasons studied from 2010-2015 they seem to follow the same type of trend in temperature during the course of the season. But when compared directly the two ways does not correlate well with each other. The best correlation is found during the seasons of 2008-09 with $R = 0.66$ and 2011-12 with $R = 0.40$, both these seasons have long periods of stable air with a peak meteor ablation height around 87-89 km after a SSW event. During the other seasons studied here the OH-airglow temperature varied more over short time spans, not giving the meteor height time to follow as it uses a couple of days to catch up to the changes. The variations in the OH-airglow temperature were also found to be large by 10-15 K than the variations in meteor height temperatures. This can come from the estimation of a stable height in the OH-airglow layer, not taking into account the movements of the layer from PWs and GWs.

Future work can be finding a method in taking the altitude of the OH-airglow layer into account, and comparing the two methods again to see if the differences are smaller. It would also be interesting to see if the OH-airglow layer height follows the same development over time as the meteor height as they are close in altitude and may be affected by the same PWs and GWs. Further see if meteor heights can be used to estimate the central height of the OH-airglow layer giving more precise OH-airglow temperatures.

Bibliography

Abe, S., Kero, J., Nakamura, T., Kastinen, D., Fujiwara, Y., Numata, S., Watanabe, J., and Hashiguchi, H. (2015). Orbit Determination of Meteoroids by MU Radar Meteor Head Echo Observations.

Bates, D. R. and Nicolet, M. (1950). The photochemistry of atmospheric water vapor. *Journal of Geophysical Research*.

Becker, E. (2012). Dynamical control of the middle atmosphere. *Space Science Reviews*.

Beig, G. (2011). Long-term trends in the temperature of the mesosphere/lower thermosphere region: 2. Solar response. *Journal of Geophysical Research: Space Physics*.

Beig, G., Scheer, J., Mlynczak, M. G., and Keckhut, P. (2008). Overview of the temperature response in the mesosphere and lower thermosphere to solar activity. *Reviews of Geophysics*.

Brasseur, G., Orlando, J. J. J. J., Tyndall, G. S. G. S. ., National Center for Atmospheric Research (U.S.), G. S. G. S., and 1955- (1999). *Atmospheric chemistry and global change*. Oxford University Press.

Dowdy, A. J., Vincent, R. A., Murphy, D. J., Tsutsumi, M., Riggin, D. M., and Jarvis, M. J. (2004). The large-scale dynamics of the mesosphere-lower thermosphere during the Southern Hemisphere stratospheric warming of 2002. *Geophysical Research Letters*.

Dyrland, M. E. (2010). *Multi-instrument studies of polar mesopause region temperature and airglow variability*. PhD thesis, University of Tromsø.

Dyrland, M. E., Hall, C. M., Mulligan, F. J., Tsutsumi, M., and Sigernes, F. (2010a). Improved estimates for neutral air temperatures at 90 km and 78°N using satellite and meteor radar data. *Radio Science*.

Dyrland, M. E., Mulligan, F. J., Hall, C. M., Sigernes, F., Tsutsumi, M., and Deehr, C. S. (2010b). Response of OH airglow temperatures to neutral air dynamics at 78°N, 16°E during the anomalous 2003-2004 winter. *Journal of Geophysical Research Atmospheres*.

Forseth, N. (2017). The Structuring of High Latitude Aurora, Master thesis.

French, J. Middle atmosphere diagram — Australian Antarctic Division.

Gavrilyeva, G. and Ammosov, P. (2018). Influence of geomagnetic activity on mesopause temperature over Yakutia. *Atmospheric Chemistry and Physics*.

Hall, C. M., Aso, T., and Tsutsumi, M. (2002). An examination of high latitude upper mesosphere dynamic stability using the Nippon/Norway Svalbard Meteor Radar. *Geophysical Research Letters*, 29(8):121–1.

Hall, C. M., Aso, T., Tsutsumi, M., Höffner, J., Sigernes, F., and Holdsworth, D. A. (2006). Neutral air temperatures at 90 km and 70°N and 78°N. *Journal of Geophysical Research*, 111(D14):D14105.

Hervig, M., Thompson, R. E., Mchugh, M., Gordley, L. L., Russell Iii, J. M., and Summers, M. E. (2001). First confirmation that water ice is the primary component of polar mesospheric clouds. *GEOPHYSICAL RESEARCH LETTERS*, 28(15):971–974.

Holmen, S. E. (2016). *Trends and variability of polar mesopause region temperatures attributed to atmospheric dynamics and solar activity*. PhD thesis, University of Tromsø.

Holmen, S. E., Dyrland, M. E., and Sigernes, F. (2014a). Long-term trends and the effect of solar cycle variations on mesospheric winter temperatures over Longyearbyen, Svalbard (78°N). *Journal of Geophysical Research*.

Holmen, S. E., Dyrland, M. E., and Sigernes, F. (2014b). Mesospheric temperatures derived from three decades of hydroxyl airglow measurements from Longyearbyen, Svalbard (78°N). *Acta Geophysica*.

Holmen, S. E., Hall, C. M., and Tsutsumi, M. (2016). Neutral atmosphere temperature trends and variability at 90km, 70 °N, 19 °E, 2003–2014. *Atmospheric Chemistry and Physics*.

Hunt, S., Oppenheim, M., Close, S., Brown, P., McKeen, F., and Minardi, M. (2004). Determination of the meteoroid velocity distribution at the Earth using high-gain radar. *Icarus*, 168(1):34–42.

Labitzke, K. (1987). SUNSPOTS, THE QBO, AND THE STRATOSPHERIC TEMPERATURE IN THE NORTH POLAR REGION. *GEOPHYSICAL RESEARCH LETTERS*, 14(5):535–537.

Lepping, R., Berdichevsky, D., and Wu, C. (2003). Sun-Earth electrodynamics: The solar wind connection. *Research Signpost*, 37(661).

Limpasuvan, V., Orsolini, Y. J., Chandran, A., Garcia, R. R., and Smith, A. K. (2016). On the composite response of the MLT to major sudden stratospheric warming events with elevated stratopause. *Journal of Geophysical Research*.

Manney, G. L., Lawrence, Z. D., Santee, M. L., Read, W. G., Livesey, N. J., Lambert, A., Froidevaux, L., Pumphrey, H. C., and Schwartz, M. J. (2015). A minor sudden stratospheric warming with a major impact: Transport and polar processing in the 2014/2015 Arctic winter. *Geophysical Research Letters*.

NASA (2018). OMNIWeb Data Explorer. *https://omniweb.gsfc.nasa.gov/form/dx1.html*.

NASA Atmospheric Chemistry and Dynamics Laboratory. Data Services: Available Annual Meteorological data. *https://acd-ext.gsfc.nasa.gov/Data_services/met/ann_data.html*.

Pedatella, N., Chau, J., Schmidt, H., Goncharenko, L., Stolle, C., Hocke, K., Harvey, V., Funke, B., and Siddiqui, T. (2018). How Sudden Stratospheric Warming Affects the Whole Atmosphere. *Eos*.

Picone, J. M., Hedin, A. E., Drob, D. P., and Aikin, A. C. (2002). NRLMSISE-00 empirical model of the atmosphere: Statistical comparisons and scientific issues. *Journal of Geophysical Research: Space Physics*, 107(A12).

Prolss, G. W. (2004). *Physics of the Earth's Space Environment: An Introduction*. Springer.

Rubin, A. E. and Grossman, J. N. (2010). Meteorite and meteoroid: New comprehensive definitions. *Meteoritics and Planetary Science*.

Schoeberl, M. R., Lait, R., Newman, P. A., and Rosenfield, J. E. (1992). The Structure of the Polar Vortex. *Journal of Geophysical Research*.

Sigernes, F., Shumilov, N., Deehr, C. S., Nielsen, K. P., Svenøe, T., and Havnes, O. (2003). Hydroxyl rotational temperature record from the auroral station in Adventdalen, Svalbard (78°N, 15°E). *Journal of Geophysical Research*, 108(A9):1342.

Sivjee, G. G. (1992). Airglow hydroxyl emissions. *Planetary and Space Science*.

Sivjee, G. G. and Hamwey, R. M. (1987). Temperature and Chemistry of the Polar Mesopause OH. *JOURNAL OF GEOPHYSICAL RESEARCH*, 92(1):4663–4672.

Straus, D. M. and Stan, C. (2009). Stratospheric predictability and sudden stratospheric warming events. *Journal of Geophysical Research Atmospheres*.

Xu, J., Smith, A. K., Wang, W., Jiang, G., Yuan, W., Gao, H., Yue, J., Funke, B., Lõpez-Puertas, M., and Russell, J. M. (2013). An observational and theoretical study of the longitudinal variation in neutral temperature induced by aurora heating in the lower thermosphere. *Journal of Geophysical Research: Space Physics*.

Yi, W., Xue, X., Chen, J., Dou, X., Chen, T., and Li, N. (2018). Estimation of Mesospheric Densities at Low Latitudes Using the Kunming Meteor Radar Together With SABER Temperatures. *Journal of Geophysical Research: Space Physics*.